Journal of Computational Physics 513 (2024) 113158

Contents lists available at ScienceDirect

Journal of Computational Physics

journal homepage: www.elsevier.com/locate/jcp

On the phase field based model for the crystalline transition and nucleation within the Lagrange multiplier framework

Qing Xia [a], Junxiang Yang [b], Junseok Kim [c], Yibao Li [a,*]

[a] School of Mathematics and Statistics, Xi'an Jiaotong University, Xi'an 710049, China
[b] School of Computer Science and Engineering, Faculty of Innovation Engineering, Macau University of Science and Technology, Macau SAR, China
[c] Department of Mathematics, Korea University, Seoul 02841, Republic of Korea

ARTICLE INFO

Keywords:
Lifshitz–Petrich model
Nucleation
Quasicrystals
Phase transition
Unconditionally stable
Phase field method

ABSTRACT

Understanding the complexity of the nucleation and transition between the crystalline and quasicrystalline is significant because the structural incommensurability is anisotropic and of significance in revealing material properties. This paper reports the two- and three-dimensional nucleation and transition investigation from quasicrystals to crystals using a phase field method. The investigation starts with the Lifshitz–Petrich (LP) model, which is derived from the Landau theory for the exploration of critical nuclei. By the variational derivation, we construct two phase field models with tenth- and eighth-order, which provide the possibility of exploring the transition under stable phase states. In order to dissipate the original Lifshitz–Petrich energy, we apply a Lagrange multiplier method to modify the two models and solve them by the Fourier spectral method. Whereas the nonlinearity leads to expensive computational burden and extra stiffness, the designed algorithm can effectively avoid the numerical oscillations caused by rigidity and keep an $O(N \log N)$ computational complexity, where N is the mesh grid size. To further demonstrate the robustness and advantages of the proposed method for handling phase-field modeling of crystalline structures, we compare its performance with other methods for constructing unconditionally stable methods. Our method can be directly implemented on a GPU for acceleration and achieves multiple times faster performance compared to CPU-only alternatives. Various numerical tests have been used to validate that our method works well for revealing the transition between different stable states during the nucleation process.

1. Introduction

Despite the quasicrystals are discovered by Shechtmann and Blech [1], the pursuits of understanding the evolution of quasicrystalline structures have never disappeared [2], whereas these explorations lead directly to a new material revolution and a tremendous progress to understand and reexamine the basic notions of matter physics [5,6]. Since the physical properties of metals and alloys are controlled by the symmetry and morphology of the crystals and quasicrystals [7], it is of great significance to quantify the transition and nucleation of quasicrystalline structure from a metastable state to a stable state for creating the desirable properties of materials [8,9]. However, various synthetic and natural compounds exhibit the periodicities and the quasiperiodicities on the metre scale [10],

* Corresponding author.
E-mail address: yibaoli@xjtu.edu.cn (Y. Li).
URL: http://gr.xjtu.edu.cn/web/yibaoli (Y. Li).

https://doi.org/10.1016/j.jcp.2024.113158
Received 27 July 2023; Received in revised form 16 May 2024; Accepted 27 May 2024

Available online 31 May 2024

which indicates that the quasicrystalline structure is not only present in metal alloys but can be exploited in diverse applications such as fabrication of photonic bandgap array [11], infrared light absorption [12], reduction of adhesion [13], heat insulation [14], and mechanical reinforcement of composites [15,16]. Archer et al. [17] started from the density functional theory to investigate a two-dimensional system of soft particles and observed the dynamic mechanism for forming quasicrystals with two length scales. They reported that the quasicrystalline structures were created by the competition between the instability of two scales. Asadi and Zaeem [18] reviewed the advancements of quantitative solid-liquid crystal modeling, which were summarized into one-mode and two-mode crystalline forms corresponding to the critical wavelength. Dotera et al. [19] theoretically explored the link between the micellar softness and the quasicrystalline order. They provided a conceptual understanding for the quasicrystals that the interactions between macromolecular particles come from contacts rather than links at a distance. Various state-of-the-art works suggested the theory of nucleation and revealed the mechanism of quasicrystal and crystal, although further studies within the computational framework are required to confirm the corresponding phenomena.

Recent developments in mechanism research of nanostructural and microstructural pattern, which plays a significant role in predicting the materials properties and reducing the experimental costs [3], have heightened the need for computational methods with high performance. Examining the nucleation and transition from the quasicrystalline structure to crystalline structure was widely concerned [4]. The methods to this issue fall in three categories of classical nucleation theory, atomistic theory, and density functional theory [5]. The classical nucleation theory is within the thermodynamic and kinetic framework [20], which describes the initial stage of the phase transformation and the decay of metastable states [21]. The atomistic theory is extended based on the classical mechanics and kinetic theory [22,23]. The density functional theory is described by the density of molecular species, whose landscape is described by a free-energy functional [24,25]. This type method investigated the properties of a system by using the electron density distribution function as the only variable describing all the corresponding properties [26,27]. Han et al. [28] established a multiscale string method to compute the minimal path of Landau–de Gennes energy and transition state. Their method demonstrated the mechanism of temperature depended energy barrier changes. Jiang and Zhang [29] focused on the high accuracy numerical method and established a projection method to compute the quasicrystalline structures rather than crystalline approximation. Cao et al. [30] developed a gradient flow based method to capture the quasiperiodic interface for the Lifshitz–Petrich model [31], which can be extended to simulate the interface dynamics between different ordered structures. Cheng et al. [32] developed and analyzed an energy stable numerical scheme for the square phase field crystal equation at the atomic scale. The theoretical analysis including unique solvability, convergence analysis, and energy stability, were provided to deepen the understanding of crystal transition from the mathematical perspective. Several previous studies [33–35] have established crystalline transition model within the phase field framework from density functional theory, which considers the interface as a thickness layer over a continuous transition.

Establishing the phase field based quasicrystalline equations was inspired by the Swift–Hohenberg equation, which is used to model the thermal fluctuation in Rayleigh–Benard convection problem [37]. Let us consider the Landau theory [36] and apply the Lifshitz–Petrich model by using the high-index saddle dynamics as follows:

$$\mathcal{E}(\phi) = \int_{\Omega} \frac{\phi}{2} L_1^2 (L_2^2 + r^2)\phi + \mathcal{F}(\phi) d\mathbf{x}, \tag{1}$$

which is established to explore the quasicrystalline structures. Here $L_1 := \nabla^2 + 1^2$ and $L_2 := \nabla^2 + q^2$ are two linear operators, the scalar order parameter $\phi(\mathbf{x}) : \Omega \subset \mathcal{R}^d (d = 2, 3) \to \mathcal{R}$ is the density profile of the molecules, ∇ is the gradient operator, 1 and q are two characteristic wavelength scales, and $\mathcal{F}(\phi) = -\epsilon\phi^2/2 - \alpha\phi^3/3 + \phi^4/4$ is the nonlinear potential. Here ϵ is denoted as a temperature-like parameter, r is denoted as a relative stable parameter of the two-mode and one-mode structure, and α is the parameter characterizing the asymmetry of the order parameters. The Lyapunov functional Eq. (1) consists a rich phase behaviors and provides the ideal model system for the investigation of transition pathways connecting crystals and quasicrystals [5]. The quadratic term $\epsilon\phi^2/2$ favors the growth of the instability [37] whereas the quartic term is responsible for its saturation by providing a lower bound for $\mathcal{E}$. The cubic term $-\alpha\phi^3/3$ is considered to modify the Lyapunov functional while the symmetry of the parametric forcing is broken and forms hexagonal patterns by taking triad interactions of standing plane waves [38].

In recent decades, a great deal of research has been devoted to the development of energy-stable numerical algorithms, which conserve the total energy of the physical system being simulated [39]. These algorithms have good stability and convergence properties, and can effectively avoid the accumulation of numerical errors. The fully implicit time discretization method treats all time terms implicitly, which can avoid the time step restriction brought by the explicit method, but the computational cost is large [40,41]. The convex splitting method split the nonlinear PDE into a set of linear or convex subproblems, which can then be easily solved [43]. The spectral method uses spectral functions to approximate spatial derivatives. While spectral methods offer advantages such as high accuracy, fast convergence, and ease of parallelization, their drawbacks, including computational expense, difficulty in handling irregular boundaries, and potential instability in certain situations, cannot be overlooked [42]. The Scalar Auxiliary Variable (SAV) method and the Invariant Energy Quadratization (IEQ) method are performed by introducing a Lagrange multiplier (auxiliary variable) [50,44]. These two kinds method have proven to be powerful to construct energy stable schemes, while they requires the integral of the free energy bounded from below. The Lagrange multiplier method introduces Lagrange multipliers to transform the energy conservation condition into a constraint condition, which is unconditionally energy stable with the original energy and does not require the explicitly treated part of the free energy to be bounded from below [45]. While these additional advantages are valuable, they do necessitate the solution of a nonlinear algebraic equation for the Lagrange multiplier. However, the computational cost of this step is negligible compared to the main cost of the algorithm, making it a worthwhile trade-off. Existing numerical methods

have been applied to study crystal nucleation under various microscopic conditions and in solid-liquid phase change scenarios, but there is a lack of research on phase transitions between different states of quasicrystals.

The aim of this paper is to develop an efficient computational method for the investigation of the nucleation and transition from quasicrystalline to crystalline within the framework of Landau theory. We establish the phase field based model by the variational derivation from the LP energy under the heuristic guidance of density functional theory, which can be used to describe the quasicrystalline structures with two characteristic wavelength scales. The derived tenth- and eighth-order model suffer from the stiffness and issues of falling into local minima caused by the nonlinear term, thus a space and time dependent Lagrange multiplier method has been applied to address these problems, which takes into account the nonlocal and local effect. In order to guarantee the second order accuracy of the algorithm, we utilize the Crank–Nicolson method in time and use the Adams–Bashforth extrapolation method to deal with the nonlinear terms. The time discretized system is analytically proved to be unconditionally energy stable, which implies that the larger time step can be used for the calculation. The additional computational cost is that the nonlinear algebraic equation for the Lagrangian multiplier can be solved by an iterative method such as Newton method with negligible computational complexity. In addition, we employ the fast Fourier spectral method in space. The computational complexity of the proposed numerical scheme is $O(N \log N)$, where N is the mesh grid size. Furthermore, our method can be performed to a GPU-accelerated discrete Fourier transform (DFT) implementation, which can be executed multiple times faster than CPU-only alternatives. Extensive numerical tests have been performed to demonstrate the accuracy and robustness of our method on investigating the nucleation and transition of quasicrystalline structure.

The outline of this paper is organized as follows. In Section 2, we briefly review the tenth- and eighth-order model by the variational derivation and introduce the Lagrange multiplier approach into the gradient flows. We develop the efficient implementation procedures based on the Fourier spectral method and the Crank-Nicolson method in Section 3. In Section 4, we present extensive numerical tests to investigate the nucleation and transition process of different quasicrystalline states. The concluding remarks are summarized in Section 5.

2. Models and the time-discretized schemes

In order to motivate the investigation on the nucleation of quasicrystals and crystals, we briefly review the variational derivation for the gradient flow dynamics. Let us denote $(\phi, \psi) = \int_\Omega \phi(\mathbf{x})\psi(\mathbf{x})d\mathbf{x}$ as the L^2 inner product between $\phi(\mathbf{x})$ and $\psi(\mathbf{x})$ and denote $\|\phi\| = (\phi, \phi)^{1/2}$ as the L^2 norm of $\phi(\mathbf{x})$.

2.1. Tenth-order model under the H^{-1} gradient flow

The dynamic governing equation can be derived by the gradient variation of the energy functional Eq. (1). Let us define the chemical potential as $\mu := \delta\mathcal{E}/\delta\phi$, thus we obtain the governing equation:

$$\phi_t = \nabla \cdot (M\nabla\mu), \tag{2a}$$

$$\mu = L_1^2\left(L_2^2 + r^2\right)\phi + \mathcal{F}'(\phi), \tag{2b}$$

where M is the constant mobility and $\mathcal{F}'(\phi) = -\epsilon\phi - \alpha\phi^2 + \phi^3$. Since Eqs. (2) are of conservative form and require no additional auxiliary variable for mass conservation, various numerical techniques have been devised to construct energy-stable schemes for gradient flows, such as the convex splitting approach [43], stabilized approach [52], Invariant energy quadratization (IEQ) approach [44], and scalar auxiliary variable (SAV) approach [50]. However, these methods are constrained by the nature of $F(\phi)$ as a high-order nonlinear term. This leads to the necessity of solving large-scale nonlinear equations (convex splitting), incorporating auxiliary variables to ensure the stability of the modified energy (IEQ, SAV), or potentially being unable to guarantee energy stability (stabilized). In order to overcome these limitations and ensure the stability of the original energy, the original model Eqs. (2) is modified with a time dependent Lagrangian multiplier $\beta(t)$ under the heuristic idea [45] as

$$\phi_t = \nabla \cdot (M\nabla\mu), \tag{3a}$$

$$\mu = L_1^2\left(L_2^2 + r^2\right)\phi + \beta(t)\mathcal{F}'(\phi), \tag{3b}$$

$$\frac{d}{dt}\int_\Omega \mathcal{F}(\phi)d\mathbf{x} = \beta(t)\int_\Omega \mathcal{F}'(\phi)\phi_t d\mathbf{x}. \tag{3c}$$

Here $\beta(t) \equiv 1$ since $\frac{d}{dt}\int_\Omega \mathcal{F}(\phi)d\mathbf{x} - \beta(t)\int_\Omega \mathcal{F}'(\phi)\phi_t d\mathbf{x} = (1-\beta(t))\frac{d}{dt}\int_\Omega \mathcal{F}(\phi)d\mathbf{x} = 0$. Due to the identity condition $\beta(t) \equiv 1$, Eqs. (3a)-(3c) are equivalent to Eqs. (2a)-(2b). The introduction of the auxiliary variable $\beta(t)$ is not intended to correct mass loss (the equation is conservative), but to forcibly dissipate the original energy. The scheme is not restricted by specific formulations of the nonlinear part within the free energy and does not require the explicitly treated part of the free energy to be bounded from below. The following energy dissipation law can be obtained:

$$\frac{d\mathcal{E}(\phi)}{dt} = -M\|\nabla\mu\|^2 \le 0, \tag{4}$$

by taking the L^2 inner products of Eq. (2a) with μ, of Eq. (2b) with ϕ_t, and integrate the equalities by parts. Thus, we construct a second order numerical schemes for Eqs. (3) based on the Crank-Nicolson method as follows:

$$\frac{\phi^{n+1}-\phi^n}{\Delta t} = \nabla\cdot(M\nabla\mu^{n+\frac{1}{2}}), \tag{5a}$$

$$\mu^{n+\frac{1}{2}} = (\Delta+1)^2\left((\Delta+q^2)^2+r^2\right)\phi^{n+\frac{1}{2}} + \beta^{n+\frac{1}{2}}\mathcal{F}'\left(\widetilde{\phi}^{n+\frac{1}{2}}\right), \tag{5b}$$

$$\left(\mathcal{F}\left(\phi^{n+1}\right)-\mathcal{F}\left(\phi^n\right),1\right) = \beta^{n+\frac{1}{2}}\left(\mathcal{F}'(\widetilde{\phi}^{n+\frac{1}{2}}),\phi^{n+1}-\phi^n\right), \tag{5c}$$

where $\widetilde{\phi}^{n+\frac{1}{2}} = (3\phi^n-\phi^{n-1})/2$. The Lagrange multiplier $\beta(t)$ can be computed by the Newton iteration. Then we can obtain the following energy dissipation law with the time discretized formation:

Theorem 1. *The numerical solutions of the numerical scheme Eqs.* (5a)-(5a) *satisfy the energy dissipative law as follows:*

$$\frac{\mathcal{E}(\phi^{n+1})-\mathcal{E}(\phi^n)}{\Delta t} = -M\left(\nabla\mu^{n+\frac{1}{2}},\nabla\mu^{n+\frac{1}{2}}\right)\le 0, \tag{6}$$

where $\mathcal{E}(\phi^{n+1}) = L_1^2(L_2^2+r^2)(\phi^{n+1})^2/2+\mathcal{F}\left(\phi^{n+1}\right)$.

Proof. Let us take the inner products of Eq. (5a) with $\mu^{n+\frac{1}{2}}$ and of Eq. (5b) with $-(\phi^{n+1}-\phi^n)/\Delta t$, and integrate the summation of multiplying Eq. (5c) with $1/\Delta t$, which leads to the following:

$$\begin{aligned}
&\frac{\mathcal{E}(\phi^{n+1})-\mathcal{E}(\phi^n)}{\Delta t}\\
&= \frac{1}{2\Delta t}(\Delta+1)^2\left((\Delta+q^2)^2+r^2\right)\left((\phi^{n+1})^2-(\phi^n)^2\right)+\frac{1}{\Delta t}\left(\mathcal{F}(\phi^{n+1})-\mathcal{F}(\phi^n)\right)\\
&= (\Delta+1)^2\left((\Delta+q^2)^2+r^2\right)\left(\phi^{n+\frac{1}{2}},\frac{\phi^{n+1}-\phi^n}{\Delta t}\right)+\beta^{n+\frac{1}{2}}\left(\mathcal{F}'\left(\widetilde{\phi}^{n+\frac{1}{2}}\right),\frac{\phi^{n+1}-\phi^n}{\Delta t}\right)\\
&= \left(\mu^{n+\frac{1}{2}},\frac{\phi^{n+1}-\phi^n}{\Delta t}\right) = -M\left(\nabla\mu^{n+\frac{1}{2}},\nabla\mu^{n+\frac{1}{2}}\right)\le 0.
\end{aligned} \tag{7}$$

This completes the proof. □

2.2. Conservative eighth-order model under the L^2 gradient flow

The supercritical instability takes the variational derivation of free energy $\mathcal{F}$ with respect to ϕ as follows:

$$\partial_t\phi = -\delta\mathcal{E}/\delta\phi = -L_1^2(L_2^2+r^2)\phi-\mathcal{F}'(\phi), \tag{8}$$

with the Neumann boundary condition $\mathbf{n}\cdot\nabla\phi=0$. However, this reaction-diffusion equation violates the law of conservation of mass. Following the method in [46], a modified model has been established by adding a nonlocal Lagrange multiplier to conserve the mass as follows

$$\frac{\partial\phi}{\partial t} = -L_1^2\left(L_2^2+r^2\right)\phi-\mathcal{F}'(\phi)+\frac{1}{|\Omega|}\int_\Omega\left(\left(q^4+r^2\right)\phi+\mathcal{F}'(\phi)\right)d\mathbf{x}. \tag{9}$$

The following mass conservation profile can be obtained as

$$\begin{aligned}
\frac{d}{dt}\int_\Omega\phi d\mathbf{x} = \int_\Omega\frac{\partial\phi}{\partial t}d\mathbf{x} = \int_\Omega\Bigg(&-L_1^2\left(L_2^2+r^2\right)\phi-\mathcal{F}'(\phi)\\
&+\frac{1}{|\Omega|}\int_\Omega\left(\left(q^4+r^2\right)\phi-\varepsilon\phi-\alpha\phi^2+\phi^3\right)d\mathbf{x}\Bigg)d\mathbf{x} = 0.
\end{aligned} \tag{10}$$

While the mass loss is spatially and temporally determined, the time-dependent Lagrangian multiplier may lead to nonlocal stiffness issue and ignore the interactions between the different lattices [47]. To overcome the dynamical difference caused by the nonlocal correction term, which has been investigated by the art-of-the-work studies [48,49], we introduce a Lagrange multiplier $\beta(t)$

$$\frac{\partial\phi}{\partial t} = -L_1^2\left(L_2^2+r^2\right)\phi+\beta(t)\Big(-\mathcal{F}'(\phi)+\frac{1}{|\Omega|}\int_\Omega(q^4+r^2)\phi+\mathcal{F}'(\phi)d\mathbf{x}\Big). \tag{11}$$

To simplify the expression, we denote

$$\mathcal{G}(\phi) = -\mathcal{F}(\phi)+\frac{1}{|\Omega|}\int_\Omega\frac{q^4+r^2}{2}\phi^2+\mathcal{F}(\phi)d\mathbf{x}. \tag{12}$$

Thus, the governing equation can be modified as

$$\frac{\partial \phi}{\partial t} = -L_1^2\left(L_2^2 + r^2\right)\phi + \beta(t)\mathcal{G}'(\phi), \tag{13a}$$

$$\frac{d}{dt}\int_\Omega \mathcal{G}(\phi)d\mathbf{x} = \beta(t)\int_\Omega \mathcal{G}'(\phi)\phi_t d\mathbf{x}, \tag{13b}$$

where $\beta(t) \equiv 1$ with the initial condition $\beta(0) = 1$. Some notations should be summarized as: (i) The Lagrangian auxiliary variables $\beta(t)$ approximately equals to 1. If we set the initial condition as $\beta(0) = 1$, then it is obvious that the modified system Eq. (13) is equivalent to Eq. (9), which indicates that $\beta(t) \equiv 1$ in the modified functional. (ii) The Lagrangian multiplier $\beta(t)$ is only activated in the interfacial region ($-1 < \phi < 1$), while it has no influence on the bulk region ($\phi = \pm 1$) [54]. The conservative eighth-order model is formulated in terms of convection-diffusion-reaction equations. Despite not being in conservative form, it still satisfies the conservation constraints, which has been analyzed as three consistency conditions in [55], i.e., consistency of reduction, consistency of mass conservation, and consistency of mass and momentum transport, respectively. (iii) Our model has transferred the nonlinear algebraic equation into the Lagrange multiplier and dissipated the original energy, which is opposed to a modified energy by taking the recently proposed SAV approach [50], IEQ approach [51], or other stabilized approaches [52,53]. Our Lagrangian multiplier based model performs the generalized behavior with the temporal and local impact, which holds the mass conservation by using the time derivation to the integral of ϕ as follows:

$$\begin{aligned}
&\frac{d}{dt}\int_\Omega \phi d\mathbf{x} = \int_\Omega \frac{\partial \phi}{\partial t} d\mathbf{x} = \int_\Omega \Big(- L_1^2\left(L_2^2 + r^2\right)\phi + \beta(t)\mathcal{G}'(\phi)\Big) d\mathbf{x} \\
&= \int_\Omega -(q^4 + r^2)\phi + \frac{d\left(\int_\Omega \mathcal{G}(\phi)d\mathbf{x}\right)/dt}{\int_\Omega \mathcal{G}'(\phi)\phi_t d\mathbf{x}}\mathcal{G}'(\phi)d\mathbf{x} \\
&= \int_\Omega -(q^4 + r^2)\phi + \left(- \mathcal{F}'(\phi) + \frac{1}{|\Omega|}\int_\Omega (q^4 + r^2)\phi + \mathcal{F}'(\phi)d\mathbf{x}\right) d\mathbf{x} = 0.
\end{aligned} \tag{14}$$

Furthermore, the governing equation satisfies the energy dissipation law by taking the L^2 inner product of Eq. (11) with ϕ_t as follows:

$$\frac{d\mathcal{E}(\phi)}{dt} = -\|\phi_t\|^2 \le 0. \tag{15}$$

We construct a second order numerical schemes for Eqs. (13) based on the Crank-Nicolson method as follows:

$$\frac{\phi^{n+1} - \phi^n}{\Delta t} = -(\Delta + 1)^2\left((\Delta + q^2)^2 + r^2\right)\phi^{n+\frac{1}{2}} + \beta^{n+\frac{1}{2}}\mathcal{G}'(\widetilde{\phi}^{n+\frac{1}{2}}), \tag{16a}$$

$$\left(\mathcal{G}(\phi^{n+1}) - \mathcal{G}(\phi^n), 1\right) = \beta^{n+\frac{1}{2}}\left(\mathcal{G}'(\widetilde{\phi}^{n+\frac{1}{2}}), \phi^{n+1} - \phi^n\right), \tag{16b}$$

where $\widetilde{\phi}^{n+\frac{1}{2}} = (3\phi^n - \phi^{n-1})/2$ is the Adams–Bashforth extrapolation. Then we can obtain the following energy dissipation law:

Theorem 2. *The numerical solutions of Eq.* (16) *satisfies the energy dissipative law,*

$$\mathcal{E}(\phi^{n+1}) - \mathcal{E}(\phi^n) = -\frac{1}{\Delta t}\left(\phi^{n+1} - \phi^n, \phi^{n+1} - \phi^n\right) \le 0, \tag{17}$$

where $\mathcal{E}(\phi^{n+1}) = L_1^2(L_2^2 + r^2)(\phi^{n+1})^2/2 + \mathcal{F}\left(\phi^{n+1}\right)$.

Proof. Let us take the L^2 inner product of $(\phi^{n+1} - \phi^n)/\Delta t$ and perform the integration by parts. Thus, we can obtain that

$$\begin{aligned}
&\mathcal{E}(\phi^{n+1}) - \mathcal{E}(\phi^n) \\
&= \frac{1}{2}(\Delta + 1)^2\left((\Delta + q^2)^2 + r^2\right)\left((\phi^{n+1})^2 - (\phi^n)^2\right) + \left(\mathcal{G}(\phi^{n+1}) - \mathcal{G}(\phi^{n+1})\right) \\
&= (\Delta + 1)^2\left((\Delta + q^2)^2 + r^2\right)\left(\phi^{n+\frac{1}{2}}, \phi^{n+1} - \phi^n\right) + \beta^{n+\frac{1}{2}}\left(\mathcal{G}'(\widetilde{\phi}^{n+\frac{1}{2}}), \phi^{n+1} - \phi^n\right)
\end{aligned} \tag{18}$$

$$= -\frac{1}{\Delta t}\left(\phi^{n+1} - \phi^n, \phi^{n+1} - \phi^n\right) \le 0, \tag{19}$$

which completes the proof. □

Before we delve into the numerical solutions and proceed with numerical validation, it is essential to provide commentary on relative advantages of the two models. It is significant for the mass conservation during the phase transition from liquid to solid crystals. The tenth-order model Eqs. (2) satisfy the mass-conserved property by taking the time derivative to the integral of ϕ over Ω, i.e.,

$$\frac{d}{dt}\int_{\Omega}\phi d\mathbf{x}=\int_{\Omega}\frac{\partial\phi}{\partial t}d\mathbf{x}=M\int_{\Omega}\Delta\mu d\mathbf{x}=M\int_{\partial\Omega}\nabla\mu\cdot\mathbf{n}ds=0, \tag{20}$$

where $\mathbf{n}$ is the unit normal vector to $\partial\Omega$. The tenth-order model includes higher order spatial derivative and this will leads to numerical problems related to efficiency, thus it is necessary to downgrade the order of differential equations, i.e., Eqs. (11), to lower computational complexity. By using the introduced Lagrange multiplier $\beta(t)$, the total mass of ϕ can be conserved. From the numerical perspective, choosing the eighth-order system brings up weaker CFL conditions for grid sizes in time and space, which reduces the complexity of solving higher-order equations. However, the modified term introduced to ensure that the eighth-order model satisfies the mass conservation property brings new challenge to the construction of fast and stable algorithms.

3. Numerical solutions

We employ the Fourier spectral method for the computation of the two high order model. The discrete systems are established in two-dimension domain $\Omega=[0,L_x]\times[0,L_y]$ for the convenience of explanation, which can be straightforward conducted to the three-dimension cases in the same manner. The computational domain is discretized with a uniform $N_x\times N_y$ mesh grid, where N_x and N_y are positive integers along the x and y direction. The space step is defined as $h=L_x/N_y=L_y/N_t$, thus the grid point is defined as $(x_j,y_k)=(jh,kh)$, where $j=0,1,\cdots,N_x-1$ and $k=0,1,\cdots,N_y-1$. Let us denote the total computational time as T and the number of time iteration as N_t, thus the time step is defined as $\Delta t=T/N_t$. We define ϕ^n_{jk} as an approximation of $\phi(x_j,y_k,n\Delta t)$ and n is the superscript n-th time level. Let us first define the discrete Fourier transform $\mathfrak{F}$ and the inverse version $\mathfrak{F}^{-1}$ as

$$\hat{\phi}^n_{pq}=\mathfrak{F}(\phi^n_{jk})=\frac{1}{N_xN_y}\sum_{j=0}^{N_x-1}\sum_{k=0}^{N_y-1}\phi^n_{jk}e^{-i(\xi_px_j+\eta_qy_k)}, \tag{21}$$

$$\phi^n_{jk}=\mathfrak{F}^{-1}(\hat{\phi}^n_{pq})=\frac{1}{N_xN_y}\sum_{p=0}^{N_x-1}\sum_{q=0}^{N_y-1}\hat{\phi}^n_{pq}e^{i(\xi_px_i+\eta_qy_j)}, \tag{22}$$

where variables ξ_p and η_q are defined as $\xi_p=2\pi j/L_x$ and $\eta_q=2\pi k/L_y$, respectively. Thus, the s-oder discrete Laplacian profiles can be recast with the discrete Fourier transformation as

$$\Delta_d^s\phi^n_{jk}=(-1)^s\frac{1}{N_xN_y}\sum_{p=0}^{N_x-1}\sum_{q=0}^{N_y-1}\left(\xi_p^2+\eta_q^2\right)^s\hat{\phi}^k_{pq}e^{i(\xi_px_j+\eta_qy_k)},\quad s=1,\cdots,4. \tag{23}$$

3.1. Discrete tenth-order model and efficient implementation

Let us denote the linear operator as $\mathcal{L}:=\Delta_d$ and $C:=(\Delta_d+1)^2\left((\Delta_d+q^2)^2+r^2\right)$, thus the discrete formulation can be implemented as

$$\frac{\phi^{n+1}-\phi^n}{\Delta t}=\mathcal{L}\mu^{n+\frac{1}{2}}, \tag{24a}$$

$$\mu^{n+\frac{1}{2}}=C\phi^{n+\frac{1}{2}}+\beta^{n+\frac{1}{2}}\mathcal{F}'\left(\widetilde{\phi}^{n+\frac{1}{2}}\right), \tag{24b}$$

$$\left(\mathcal{F}\left(\phi^{n+1}\right)-\mathcal{F}\left(\phi^n\right),1\right)_d=\beta^{n+\frac{1}{2}}\left(\mathcal{F}'\left(\widetilde{\phi}^{n+\frac{1}{2}}\right),\phi^{n+1}-\phi^n\right)_d, \tag{24c}$$

where $\widetilde{\phi}^{n+\frac{1}{2}}=(3\phi^n-\phi^{n-1})/2$.

Solutions for discrete system Eqs. (24a)-(24c).

Let us derive from Eqs. (24a)-(24c) that

$$\frac{\phi^{n+1}}{\Delta t}-\frac{\mathcal{L}C}{2}\phi^{n+1}=\frac{\phi^n}{\Delta t}+\frac{\mathcal{L}C}{2}\phi^n+\mathcal{L}\mathcal{F}'\left(\widetilde{\phi}^{n+\frac{1}{2}}\right)\beta^{n+\frac{1}{2}}. \tag{25}$$

By defining the linear operator $\mathcal{X}(\phi):=(I/\Delta t-\mathcal{L}C/2)\phi$ and applying the inverse operator $\mathcal{X}^{-1}$ to both sides of Eq. (25), we can obtain that

$$\phi^{n+1}=\mathcal{A}_1^{n+1}+\beta^{n+\frac{1}{2}}\mathcal{B}_1^{n+1}, \tag{26a}$$

$$\text{with}\quad \mathcal{A}_1^{n+1}:=\frac{1}{\Delta t}\mathcal{X}^{-1}(\phi^n)+\frac{1}{2}\mathcal{X}^{-1}\left(\mathcal{L}C\phi^n\right)\quad\text{and}\quad \mathcal{B}_1^{n+1}:=\mathcal{X}^{-1}\left(\mathcal{L}\mathcal{F}'\left(\widetilde{\phi}^{n+\frac{1}{2}}\right)\right). \tag{26b}$$

Then let us take Eq. (26b) into Eq. (24c) for solving $\beta^{n+\frac{1}{2}}$ as follows:

$$\left(\mathcal{F}\left(\mathcal{A}_1^{n+1}+\beta^{n+\frac{1}{2}}\mathcal{B}_1^{n+1}\right)-\mathcal{F}\left(\phi^n\right),1\right)=\beta^{n+\frac{1}{2}}\left(\mathcal{F}'\left(\widetilde{\phi}^{n+\frac{1}{2}}\right),\mathcal{A}_1^{n+1}+\beta^{n+\frac{1}{2}}\mathcal{B}_1^{n+1}-\phi^n\right)_d, \tag{27}$$

which is a fourth-order nonlinear algebraic equation for $\beta^{n+\frac{1}{2}}$ and can be solved by the Newton iterative method. It should be pointed out that our purpose is to find the approximate solutions around $\beta^{n+\frac{1}{2}}=1$, which is simple with lower computation cost if we use $\beta^0=1$ as the initial condition. With the updated β^{n+1}, we can obtain ϕ^{n+1} by solving Eq. (26a).

3.2. Discrete and conservative eighth-order model and efficient implementation

The discrete formulation for Eq. (9) can be implemented as

$$\frac{\phi^{n+1}-\phi^n}{\Delta t}=-C\phi^{n+\frac{1}{2}}+\beta^{n+\frac{1}{2}}\mathcal{G}'(\widetilde{\phi}^{n+\frac{1}{2}}), \tag{28a}$$

$$\left(\mathcal{G}(\phi^{n+1})-\mathcal{G}(\phi^n),1\right)_d=\beta^{n+\frac{1}{2}}\left(\mathcal{G}'(\widetilde{\phi}^{n+\frac{1}{2}}),\phi^{n+1}-\phi^n\right)_d, \tag{28b}$$

where $\widetilde{\phi}^{n+\frac{1}{2}}=(3\phi^n-\phi^{n-1})/2$.

Solutions for discrete system Eqs. (28a)-(28b).

Let us derive from Eqs. (28a)-(28b) that

$$\frac{\phi^{n+1}}{\Delta t}+\frac{C}{2}\phi^{n+1}=\frac{\phi^n}{\Delta t}-\frac{C}{2}\phi^n+\beta^{n+\frac{1}{2}}\mathcal{G}'(\widetilde{\phi}^{n+\frac{1}{2}}). \tag{29}$$

Then we define the linear operator $\mathcal{Y}(\phi):=(I/\Delta t+C/2)\phi$ and apply the inverse operator $\mathcal{Y}^{-1}$ to both sides of Eq. (25), which leads to the follows:

$$\phi^{n+1}=\mathcal{A}_2^{n+1}+\beta^{n+\frac{1}{2}}\mathcal{B}_2^{n+1}, \tag{30a}$$

$$\phi^{n+1,\star}=\mathcal{A}_2^{n+1}+\mathcal{B}_2^{n+1}, \tag{30b}$$

$$\text{with}\quad \mathcal{A}_2^{n+1}:=\frac{1}{\Delta t}\mathcal{Y}^{-1}(\phi^n)-\frac{1}{2}\mathcal{Y}^{-1}\left(C\phi^n\right)\quad\text{and}\quad \mathcal{B}_2^{n+1}:=\mathcal{Y}^{-1}\left(\mathcal{G}'(\widetilde{\phi}^{n+\frac{1}{2}})\right). \tag{30c}$$

Then we provide two methods to update $\beta^{n+\frac{1}{2}}$:

Method 1. Let us take Eq. (30a) into Eq. (28b) as follows:

$$\left(\mathcal{G}(\mathcal{A}_2^{n+1}+\beta^{n+\frac{1}{2}}\mathcal{B}_2^{n+1})-\mathcal{G}(\phi^n),1\right)=\beta^{n+\frac{1}{2}}\left(\mathcal{G}'(\widetilde{\phi}^{n+\frac{1}{2}}),\mathcal{A}_2^{n+1}+\beta^{n+\frac{1}{2}}\mathcal{B}_2^{n+1}-\phi^n\right)_d. \tag{31}$$

By solving the nonlinear functional Eq. (31) with $\beta^0=1$ based on the Newton iterative method, we can calculate $\beta^{n+\frac{1}{2}}$. The iterative method used for the computation of Eq. (27) is efficient and the computational burden is negligible by taking $\beta^0=1$ as the initial condition.

Method 2. Let us take $\phi^{n+1,\star}$ into Eq. (28b) for solving $\beta^{n+\frac{1}{2}}$ as follows:

$$\left(\mathcal{G}(\phi^{n+1,\star})-\mathcal{G}(\phi^n),1\right)=\beta^{n+\frac{1}{2}}\left(\mathcal{G}'(\widetilde{\phi}^{n+\frac{1}{2}}),\phi^{n+1,\star}-\phi^n\right)_d. \tag{32}$$

By solving an explicit functional Eq. (32), we can calculate $\beta^{n+\frac{1}{2}}$. It should be remarked that $\mathcal{G}(\phi)$ is highly nonlinear and brings expensive computational complexity for the calculation comparing to $\mathcal{F}(\phi)$ in Eq. (27). Thus, $\phi^{n+1,\star}$ is defined as the intermediate variable for the explicit computation of $\beta^{n+\frac{1}{2}}$. After updating $\beta^{n+\frac{1}{2}}$ by **Method 1** or **Method 2**, we can solve ϕ^{n+1} by recalculating Eq. (30a).

Several important notations should be pointed out here: (i) The Allen-Cahn type equation satisfies the maximum principle as discussed in the existing literature [57]. In Eq. (13), we introduce a finite Lagrangian term to the eighth-order model in order to conserve mass, without affecting the solutions that satisfy the maximum bound principle [58]. Therefore, the solution of Eq. (13) is bounded, and the bound is affected by the parameters ϵ and α in the polynomial function $\mathcal{F}(\phi)$. The space-time Lagrange multiplier, which employs the Karush-Kuhn-Tucker conditions as a constraint, ensures the preservation of positivity within bounds. (ii) While the maximum bound principle akin to the Allen–Cahn equation has not been formally established for the Cahn–Hilliard type equation, the boundedness of solutions for this type of equation can be explored [61]. As the negative biharmonic operator in the Cahn–Hilliard type equation is not negative diagonally dominant like the Laplace operator in the Allen–Cahn equation, the upwind-convex splitting method, presented in reference [62], provides an original structure-preserving scheme. Therefore, the boundedness of the solution of the tenth-order model in Eq. (3) can be verified using the upwind-convex splitting method proposed in reference [59]. For more comprehensive information, the reader is referred to [60].

4. Numerical validations

In this section, we implement various tests to verify the efficiency of the proposed method and reveal the transition pathways during the nucleating process. We first investigate the comparison effect of various numerical methods with the proposed method.

Then we demonstrate the phase diagram of different stable states in 2D $\epsilon - \alpha$ plane. Furthermore, we perform the quantitative measurements on the energy dissipation and mass error estimate. Additionally, we demonstrate the stable quasicrystalline and crystalline pattern in 3D space and the transition pathway between different state. Unless otherwise specified, the following parameters are chosen for the computation: $r = 0.01$, $q = 2\cos(\pi/12)$, $h = 0.5$ and $\Delta t = 0.1h$.

4.1. Comparison and verification of various numerical methods

In this subsection, we investigate the comparison effect by taking various methods, i.e., the Crank-Nicolson based implicit method, IEQ method, SAV method, and the proposed Lagrange multiplier method, respectively. The Crank-Nicolson based implicit time discretization method overcomes the limitation of time step size, but at the expense of significantly increased computational cost. Furthermore, it is hard to propose the unconditionally stable numerical algorithm. The IEQ method necessitates by solving linear equations with intricate variable coefficients and imposes the constraint that the free energy density must be bounded. The SAV method improves upon the IEQ method by relaxing the requirements for the energy density function. However, it still requires the integral of the nonlinear functional in the free energy to be bounded from below. It is important to emphasize that both the SAV and IEQ methods operate on a modified energy rather than the original energy. The Lagrange multiplier method inherits most of the advantages of the SAV and IEQ methods, and it also avoids the requirement for the boundedness of the energy density functional. However, it comes with a drawback of solving a linear equation with a small computational cost. Taking the eight-order equation as an example, we first establish the discrete systems of these algorithms based on the Crank-Nicolson method as follows:

$$\text{Crank-Nicolson-based implicit:}\quad \begin{aligned}\frac{\phi^{n+1}-\phi^n}{\Delta t} &= -(\Delta+1)^2\left((\Delta+q^2)^2+r^2\right)\phi^{n+\frac{1}{2}} \\ &\quad - \mathcal{F}'(\phi^{n+\frac{1}{2}}) + \frac{1}{|\Omega|}\int_\Omega \left(q^4+r^2\right)\phi^{n+\frac{1}{2}} + \mathcal{F}'\left(\phi^{n+\frac{1}{2}}\right)d\mathbf{x}.\end{aligned} \tag{33}$$

$$\text{IEQ:}\quad \begin{cases} \dfrac{\phi^{n+1}-\phi^n}{\Delta t} + (\Delta+1)^2\left((\Delta+q^2)^2+r^2\right)\phi^{n+\frac{1}{2}} + \dfrac{\mathcal{F}'(\phi^{n+\frac{1}{2}})}{\sqrt{\mathcal{F}(\phi^{n+\frac{1}{2}})+C_{IEQ}}}u^{n+\frac{1}{2}} \\ \qquad - \dfrac{1}{|\Omega|}\displaystyle\int_\Omega\left(\left(q^4+r^2\right)\phi^{n+\frac{1}{2}} + \dfrac{\mathcal{F}'(\phi^{n+\frac{1}{2}})}{\sqrt{\mathcal{F}(\phi^{n+\frac{1}{2}})+C_{IEQ}}}u^{n+\frac{1}{2}}\right)d\mathbf{x} = 0, \\ u^{n+1}-u^n = \dfrac{\mathcal{F}'(\phi^{n+\frac{1}{2}})(\phi^{n+1}-\phi^n)}{2\sqrt{\mathcal{F}(\phi^{n+\frac{1}{2}})+C_{IEQ}}}. \end{cases} \tag{34}$$

Here, $v(t,\phi) = \sqrt{\mathcal{F}(\phi)+C_{IEQ}}$ is the auxiliary variable, where C_{IEQ} is a positive constant that ensures $\mathcal{F}(\phi) \geq -C_{IEQ}$.

$$\text{SAV:}\quad \begin{cases} \dfrac{\phi^{n+1}-\phi^n}{\Delta t} + (\Delta+1)^2\left((\Delta+q^2)^2+r^2\right)\phi^{n+\frac{1}{2}} + \dfrac{\mathcal{F}'(\phi^{n+\frac{1}{2}})}{\sqrt{\int_\Omega \mathcal{F}(\phi^{n+\frac{1}{2}})d\mathbf{x}+C_{SAV}}}v^{n+\frac{1}{2}} \\ \qquad - \dfrac{1}{|\Omega|}\displaystyle\int_\Omega\left(\left(q^4+r^2\right)\phi^{n+\frac{1}{2}} + \dfrac{\mathcal{F}'(\phi^{n+\frac{1}{2}})}{\sqrt{\int_\Omega \mathcal{F}(\phi^{n+\frac{1}{2}})dx+C_{SAV}}}v^{n+\frac{1}{2}}\right)d\mathbf{x} = 0, \\ v^{n+1}-v^n = \dfrac{\int_\Omega \mathcal{F}'(\phi^{n+\frac{1}{2}})(\phi^{n+1}-\phi^n)d\mathbf{x}}{2\sqrt{\int_\Omega \mathcal{F}(\phi^{n+\frac{1}{2}})d\mathbf{x}+C_{SAV}}}. \end{cases} \tag{35}$$

Here, $v(t) = \sqrt{\int_\Omega \mathcal{F}(\phi)d\mathbf{x}+C_{SAV}}$ is the scalar auxiliary variable, where C_{SAV} is a positive constant that ensures $\int_\Omega \mathcal{F}(\phi)dx \geq -C_{SAV}$.

To conduct a rigorous comparative analysis of the efficacy of these four numerical algorithms, we have instantiated the simulation with identical stochastic initial conditions to ascertain the veracity of the nucleation state in the crystallization process. The data presented in Fig. 1 illustrate the configurations at the final computational time $T = 10$. A critical examination of the results reveals that the delineation of the crystal interface, as demarcated by the red contours, exhibits varying degrees of precision and acuity against the blue backdrop representing the crystal matrix. Notably, the interface delineated by the proposed Lagrange multiplier method (Fig. 1(d)) manifests with pronounced sharpness and definition, suggesting its superior capability in capturing intricate interface details with heightened accuracy. Upon scrutinizing the homogeneity of the blue crystal lattice, it is discernible that the configurations engendered by both the Crank-Nicolson based implicit method (Fig. 1(a)) and our proposed method (Fig. 1(d)) are characterized by a more consistent and orderly pattern. In contrast, the structures portrayed by the IEQ (Fig. 1(b)) and SAV (Fig. 1(c)) methods betray minor anomalies within certain locales. In the ideal scenario of a phase transition, the crystal lattice is expected to

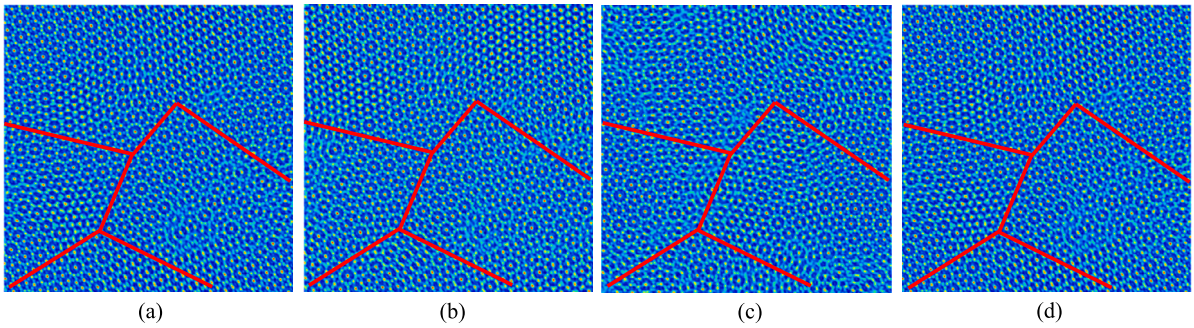

Fig. 1. Different crystalline phase transition by taking four different methods with the same parameters: (a) the Crank-Nicolson based implicit (CNI) method, the invariant energy quadratization (IEQ) method, the scalar auxiliary variable (SAV) method, (d) our proposed Lagrange multiplier method (Ours). (For interpretation of the colors in the figure(s), the reader is referred to the web version of this article.)

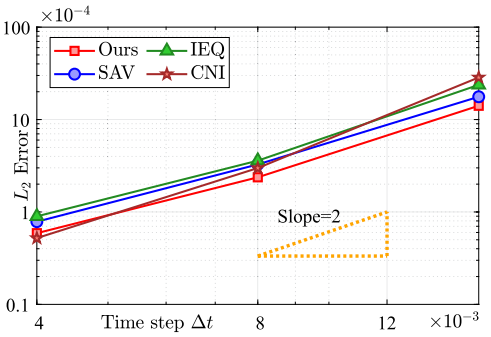

Fig. 2. The L^2 numerical errors at $T = 1$ for the approximate phase variable ϕ of the presumed exact solution Eq. (36), that are computed using for different numerical method.

evince a certain symmetry. An analysis of the results indicates that while all methods approximate this symmetry to some extent, the Crank-Nicolson based implicit method and our Lagrange multiplier method are distinguished by their more faithful representation of symmetric structures. Moreover, the simulation results attributable to the Lagrange multiplier method suggest a superior degree of smoothness and continuity, a metric by which the alternative methods also deliver satisfactory performance. Each algorithm exhibits its unique attributes and strengths. Our proposed method is distinguished by its discernible advantages in the clarity of the interface, the uniformity of structural patterns, and the maintenance of symmetry and smoothness. A detailed numerical error analysis is requisite for the derivation of more definitive quantitative assessments of these observations.

We assume the following function

$$\phi(x, y, t) = \sin(x)\cos(y)\cos(t), \tag{36}$$

to be the exact solution and impose some suitable force fields such that the given solution can satisfy the system (11). We compare the results obtained by using Eqs. (33), (34), (35), and (16) as shown in Fig. 2. We present the L^2 error profiles for the phase variable ϕ, contrasting the numerically simulated solutions with the analytical benchmarks at $T = 1$ across a spectrum of temporal discretizations. The graphical elucidation of the results indicates that our method manifests the most diminutive error, signifying its superlative precision in the context of this examination. The errors associated with the IEQ and SAV methods are observed to be in close contention, whereas the Crank-Nicolson implicit approach incurs the most substantial error magnitude. Notwithstanding the elevated error associated with the Crank-Nicolson implicit scheme, the error augmentation trajectories with escalating time steps demonstrate a relative uniformity amongst the investigated methods. This uniformity implies that the stability of the methods may be deemed acceptable within the scrutinized temporal resolution domain. It is imperative to acknowledge that the incorporation of an auxiliary variable in both the SAV and IEQ methods necessitates the establishment of a lower bound for the integral of the free energy functional. Although the polynomial function $\mathcal{F}$ is intrinsically bounded, this is contingent on the parameters α and ϵ, which are pivotal in delineating the phase transition between crystal states and the nexus of energy to nucleation phenomena. Consequently, the selection of an auxiliary variable for the SAV or IEQ methods poses a significant challenge, as it is requisite to ascertain a meaningful lower bound that confers validity to the auxiliary construct.

4.2. The phase transition of different stable order parameters in 2D dimension

In this subsection, we perform the quasiperiodic structure with periodic boundary conditions in a square domain by taking the pseudospectral method. The computation is performed with the eighth-order model Eqs. (13) under the L^2 gradient flow. The computational domain is set as $\Omega = [0, 256] \times [0, 256]$ with a 512×512 mesh grid. The initial conditions are chosen as

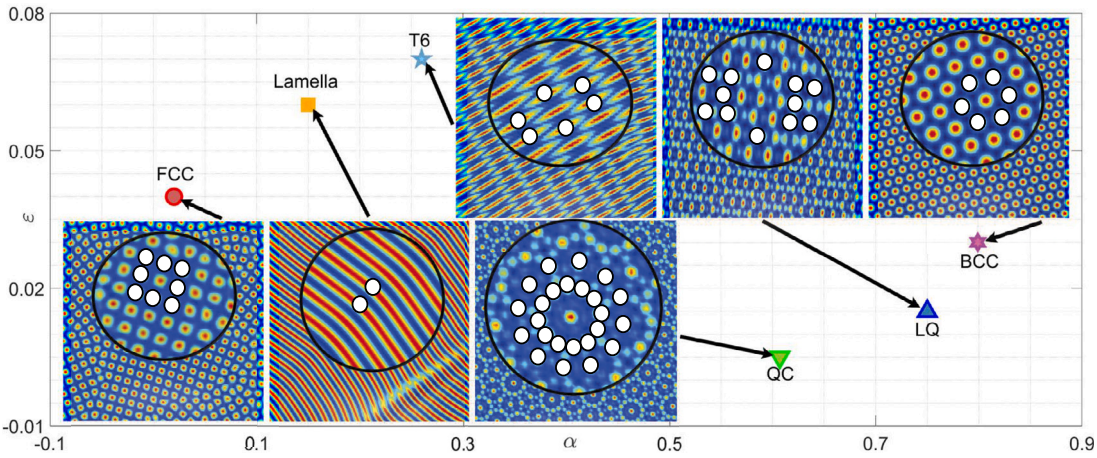

Fig. 3. Various specific stable ordered states, such as FCC, Lamella, T6, QC, LQ, and BCC and the corresponding phase diagram under different parameter combinations in 2D space. The x-axis is the range of ϵ and the y-axis is the range of α. The inset figures circled by the black lines are the close-up views of different indicated crystalline states in real space. The schematic diagrams of prominent diffraction patterns in the reciprocal space have been demonstrated by the spatial combinations of white solid circles based on the real space patterns.

$$\phi(x, y, 0) = \bar{\phi} + 0.01\text{rand}(x, y), \tag{37}$$

where rand(**x**) is the random number between -1 and 1. The unit cell is generally chosen to hold about 40 wavelengths in the computational region. Different stable order parameter solutions within inhomogeneous state can be obtained by the proposed method, including 6-fold face centered cubic (FCC), Lamella state, 12-fold quasicrystalline state (QC), transformed 6-fold crystalline state (T6), lamellar quasicrystalline state (LQ), and 6-fold body centered cubic (BCC). Note that in addition to classical crystalline states with global symmetry and periodicity, such as FCC, BCC, Lamella, and QC, there are other stable states (LQ and T6) with local symmetry and quasiperiodicity that cannot be neglected. We have plotted the specific stable order parameter in the $\epsilon - \alpha$ plane as can be seen from Fig. 3. For this simulation, we apply $\bar{\phi} = 0$ for Lamella, T6, QC, and LQ, and apply $\bar{\phi} = -0.25$ for FCC and BCC. The sub-figures in Fig. 3 show the stable structures in real and it reciprocal spaces with different combinations of (α, ϵ) as FCC (0.01, 0.04), Lamella (0.15, 0.06), QC (0.6, 0.005), T6 (0.26, 0.07), LQ (0.75, 0.015), and BCC (0.8, 0.03), respectively. What we should point out is that this result demonstrates several stable states with special parameters combinations during the examination of our proposed algorithm. Our method works well for the construction of quasicrystalline and crystalline structures. The generality of the Lifshitz-Petrich model Eq. (1) guarantees that more complicated stable patterns can be discovered by traversing all parameter combinations and amplitudes. Furthermore, we plot the close-up views of different indicated crystalline states in the inset figures circled by the black lines in real space. The schematic diagrams of prominent diffraction patterns in the reciprocal space have demonstrated by the spatial combinations of white solid circles based on the real space patterns, which is obtained by the absolute value of the Fourier-transformed density [56].

4.3. Energy stability and mass conservation

In this section, we perform the numerical investigation on the above crystalline states in Fig. 3. We demonstrate the numerical energy dissipation based on the tenth-order scheme in Fig. 4 and the eighth-order scheme in Fig. 5, respectively. We compute the time evolution of the normalized discrete energy $\mathcal{E}(\phi^n)/\mathcal{E}(\phi^0)$. We choose the same initial conditions and parameter settings as those in Section 4.2. As can be seen from Fig. 4 and Fig. 5, it is obvious that the time discretized energy curves of the above six cases are indeed non-increasing, which corresponds to the proposed Theorem 1 and Theorem 2. Therefore, this phenomenon indicates that our algorithm can guarantee the original energy dissipates, which means that large time steps can be applied to the computation. We should provide some explanations for the differences between Fig. 4 and 5. It can be seen that a jump-type transitional effect for the eighth-order model. This phenomenon is attributed to the complexity within the system. In complex nonlinear systems, the dissipation of energy may be influenced by various factors such as random initial conditions, interactions, and the characteristics of the dissipation process. The complexity of these factors may result in non-monotonic behavior or highly jump-type transitions in the temporal variation of the energy function. The highly variable energy involved in the phase transition of quasicrystals from a physical perspective is not discussed within the scope of this paper. The mass conservation is the basic property during the crystalline transition and nucleation, which requires us to investigate whether the proposed numerical scheme satisfies this property. Let us define the mass error during the evolution as the discrete l_2-norm as the following functional:

$$e^n = \sqrt{\sum_{i=1}^{N_x}\sum_{j=1}^{N_y} \phi_{i,j}^n/(N_x N_y) - \sum_{i=1}^{N_x}\sum_{j=1}^{N_y} \phi_{i,j}^0/(N_x N_y)}, \tag{38}$$

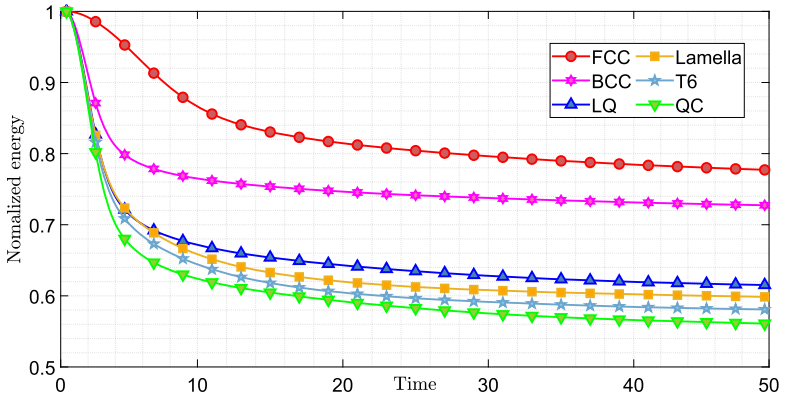

Fig. 4. Temporal evolution of the non-increasing discrete energy by taking the eighth-order scheme (Eq. (24)) with different quasicrystalline and crystalline states, i.e., FCC, BCC, LQ, Lamella, T6, and QC. Note that the total energy has been normalized by the initial energy. The time step used for this investigation is $\Delta t = 0.01h$.

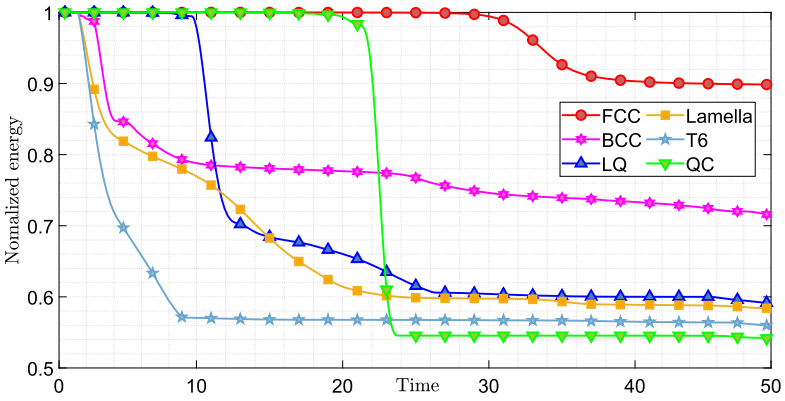

Fig. 5. Temporal evolution of the non-increasing discrete energy by taking the eighth-order scheme (Eq. (28)) with different quasicrystalline and crystalline states, i.e., FCC, BCC, LQ, Lamella, T6, and QC. Note that the total energy has been normalized by the initial energy. The time step used for this investigation is $\Delta t = 0.01h$.

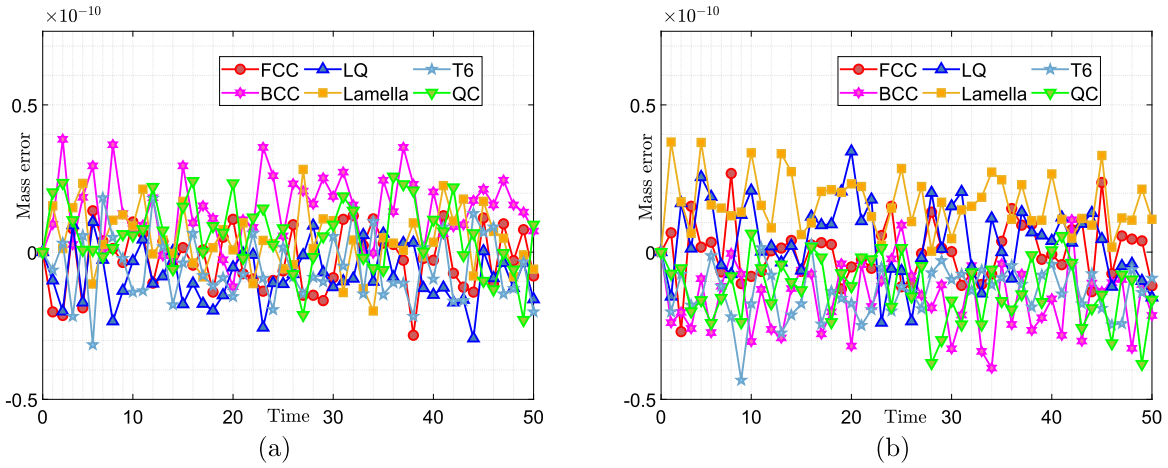

Fig. 6. Time evolution of the mass error obtained by (a) tenth-order scheme and (b) eighth-order scheme with different quasicrystalline and crystalline states, i.e., FCC, BCC, LQ, Lamella, T6, and QC.

which considers the difference between the mass density at the n-th step and the initial mass density. We apply the two crystalline state model to estimate the mass errors during the evolution process, which can be seen from Fig. 6. In general, the comparison results demonstrate that the mass error of our algorithm is within the acceptable range.

Table 1
Convergence rate and l_2 error of the tenth-order and eighth-order schemes. The time step $\Delta t = 0.1h$ is chosen for the proposed numerical schemes.

h	Tenth-order scheme		Eighth-order scheme	
	l_2 error	Rate	l_2 error	Rate
0.1	3.846×10^{-4}		3.107×10^{-4}	
0.05	9.122×10^{-5}	2.08	7.217×10^{-5}	2.11
0.025	2.197×10^{-5}	2.06	1.682×10^{-5}	2.10
0.0125	5.207×10^{-6}	2.08	4.065×10^{-6}	2.05

4.4. Convergence tests

In this section, we perform the convergence test, by considering the Cauchy error, to verify the second-order accuracy of our proposed method by using various simulations with increasingly finer mesh grid $h = 1, 0.5, 0.25$, and 0.125 in the same computational domain $\Omega = [0, 64] \times [0, 64]$. Note that the Cauchy Error, which is defined as the difference between any two terms of a sequence and not with the exact solution, is widely used to measure the error without knowing the exact solution. Furthermore, the accuracy of the algorithm can be scrutinized by employing the manufactured solutions approach. This method commences by assuming an analytic solution, from which an artificial "true" solution is constructed, enabling the validation of computed outcomes [55]. We have chosen to use the Cauchy error criterion since it allows us to avoid the need to assume an accurate solution beforehand and evade a great deal of post-processing work to validate the calculated results. The initial conditions are chosen as follows:

$$\phi(x, y, 0) = 0.25 + 0.25\sin(2\pi x)\sin(2\pi y), \tag{39}$$

and the time step is set as $\Delta t = 0.1h$. Thus, the crystalline phase separation will be performed under the initial conditions. Due to the absence of analytical solutions, let us assume that the reference solution obtained by the fine spatial step $h =$ 1e-3 with a fine temporal step $\Delta t =$ 1e-4. By defining the error of the numerical scheme as the discrete l_2-norm of the difference between the corresponding grid and the reference solutions cells neighboring it, i.e., $e_{h,\,\Delta t} := \phi_{h,\,\Delta t} - \phi^{\mathbf{ref}}$, thus we can define the convergence ratio of the successive errors as $\log_2\left(\|e_{h,\,\Delta t}\|_2 / \|e_{h/2,\Delta t/2}\|_2\right)$. For the tenth-order scheme and the eighth-order scheme, we apply the numerical method over time $T = 50$ with $\Delta t = 0.1h$ under each grid, respectively. The ratio of the numerical errors is 2 since $\|e_{h,\,\Delta t}\|_2 = O(h^2)$ is defined and $\Delta t = 0.1h$ is chosen for the error estimate. The l_2 errors and the convergence ratios are listed in Table 1, respectively. The numerical results suggest that the discrete schemes of Eq. (24) and Eq. (28) are both second-order accurate in space and time, which corresponds to the expected discretization.

4.5. The phase transition of different stable order parameters in 3D dimension

In order to demonstrate the possible three-dimensional equilibrium phase structure, we have performed the proposed procedure on the crystalline generation as shown in Fig. 7, which is plotted by the 3D order parameters. We take the eighth-order model Eqs. (13) as the example to illustrate the results in $\alpha - \epsilon$ plane. The computational domain is chosen as $\Omega = [0, 50] \times [0, 50] \times [0, 50]$ with a $100 \times 100 \times 100$ mesh grid. We design the unit computational cell to hold about 20 wavelengths. The initial conditions are chosen as

$$\phi(x, y, z, 0) = \bar{\phi} + 0.1\mathrm{rand}(x, y, z), \tag{40}$$

for the six cases, where $\mathrm{rand}(x, y, z)$ is the random number between -1 and 1. We choose the same parameters as that in Sec. 4.2. For the three dimensional simulation, we apply $\bar{\phi} = 0$ for Lamella, T6, QC, and LQ, and apply $\bar{\phi} = -0.1$ for FCC and BCC. As can be seen from Fig. 7, we have demonstrated the three-dimensional pattern in the $\alpha - \epsilon$ plane. For each indicated crystalline state, the left sub-figure shows the snapshot of the iso-surface of $\{\phi = -0.1\}$, and the right sub-figure shows the perpendicular cross-sections on the surfaces of the cubic computational domain. The sub-figures in Fig. 7 show the stable structures in real and reciprocal spaces with different combinations of (α, ϵ) as FCC (0.02, 0.03), Lamella (0.11, 0.068), QC (0.65, 0.008), T6 (0.22, 0.064), LQ (0.78, 0.011), and BCC (0.82, 0.037), respectively. As can be seen from the results of the $\{\phi = -0.1\}$ iso-surface, we can obviously see that the stable order crystalline structures have been obtained by our proposed method. In order to confirm the three-dimensional results, we have demonstrated three perpendicular cross-sections on the surfaces of the unit cubic domain. By comparing the results, we can realize that although there are differences in symmetry and rotation patterns between two- and three-dimensional structures, which are caused by the fluctuations in different thermodynamics, we can obviously see the periodic and symmetrical crystalline pattern by projecting onto the surface of the unit cubic domain.

4.6. The transition pathway between specific transient state

In this subsection, we demonstrate the transition pathway between different quasicrystalline and crystalline stable states as shown in Fig. 8 and Fig. 9. The sub-figures demonstrate the phase patterns of corresponding crystallines in 3D space and the projected patterns in 2D plane. The transferred energy is denoted as $\Delta\mathcal{E}$, whose positive value represents the energy that needs to be absorbed

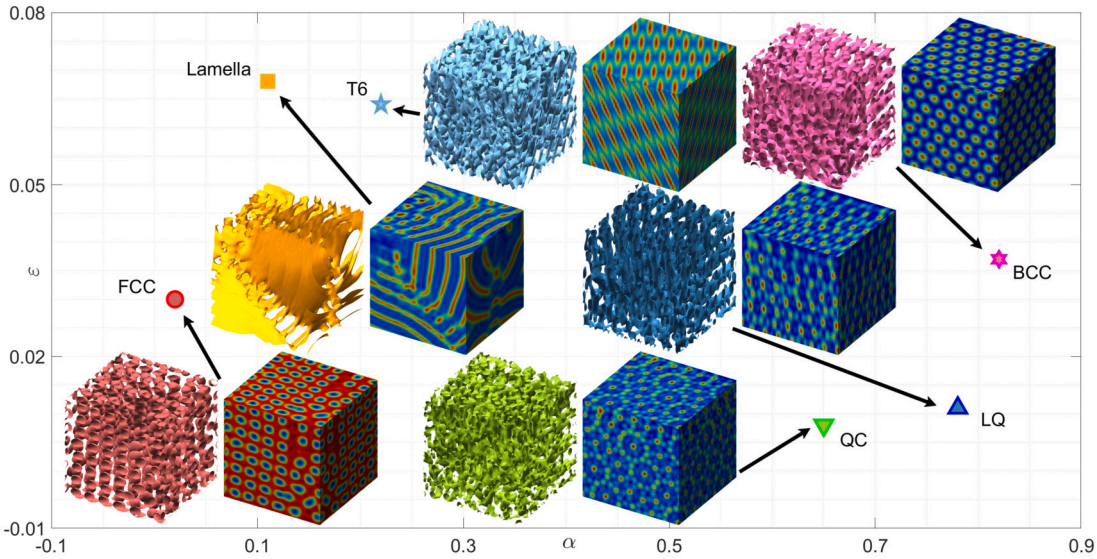

Fig. 7. Various specific stable ordered states, such as FCC, Lamella, T6, QC, LQ, and BCC and the corresponding phase diagram under different parameter combinations in 3D space. The x-axis is the range of ϵ and the y-axis is the range of α. For each indicated crystalline state, the left sub-figure shows the snapshot of the iso-surface of $\{\phi = -0.1\}$, the right sub-figure shows the perpendicular cross-sections on the surfaces of the cubic computational domain.

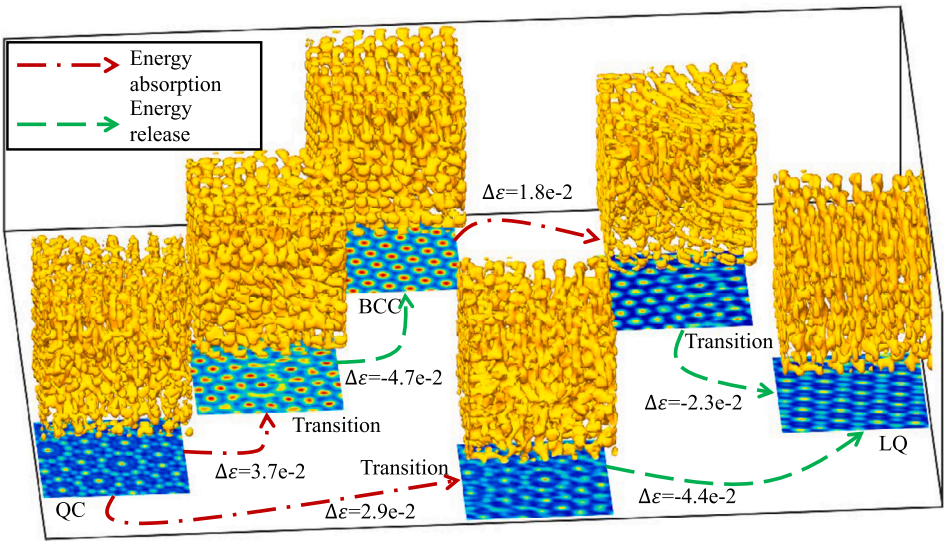

Fig. 8. Dynamic behaviors and transition pathways between different stable order states, including QC to BCC, BCC to LQ, and QC to LQ, respectively. The sub-figures demonstrate the phase patterns of corresponding crystalline states in 3D space and the projected patterns in the 2D plane. The transferred energy is denoted as $\Delta\mathcal{E}$, whose positive value represents the energy that needs to be absorbed for the transition, and vice versa. The red dashed-dot lines represent the direction of transition caused by the energy absorption and the green dashed lines represent the direction of transition caused by the energy release.

for the transition, and vice versa. The red dashed-dot lines represent the direction of transition caused by the energy absorption and the green dashed lines represent the direction of transition caused by the energy release. As can be seen from the results, it is obvious that the transition requires absorbing energy to be metastable and release the energy to reconstruct novel crystalline structures, which corresponds to Ostwald's step rule [63]. As can be seen from Fig. 8, we can obtain the following three transition pathways: (i) From QC state to the BCC state by absorbing energy $\Delta\mathcal{E} = 3.7\text{e-}2$ and releasing the energy $\Delta\mathcal{E} = 4.7\text{e-}2$ with $(\alpha, \epsilon) = (0.95, 0.05)$. (ii) From BCC state to the LQ state by absorbing energy $\Delta\mathcal{E} = 1.8\text{e-}2$ and releasing the energy $\Delta\mathcal{E} = 2.3\text{e-}2$ with $(\alpha, \epsilon) = (0.7, 0.017)$. (iii) From QC state to the LQ state by absorbing energy $\Delta\mathcal{E} = 2.9\text{e-}2$ and releasing the energy $\Delta\mathcal{E} = 4.4\text{e-}2$ with $(\alpha, \epsilon) = (0.82, 0.024)$. As can be seen from Fig. 9, we can obtain the following three transition pathways: (i) From QC state to the T6 state by absorbing energy $\Delta\mathcal{E} = 1.9\text{e-}2$ and releasing the energy $\Delta\mathcal{E} = 2.3\text{e-}2$ with $(\alpha, \epsilon) = (0.35, 0.05)$. (ii) From T6 state to the Lamella state by absorbing energy $\Delta\mathcal{E} = 3.3\text{e-}2$ and releasing the energy $\Delta\mathcal{E} = 3.7\text{e-}2$ with $(\alpha, \epsilon) = (0.18, 0.07)$. (iii) From QC state to the Lamella state by absorbing energy $\Delta\mathcal{E} = 1.6\text{e-}2$ and releasing the energy $\Delta\mathcal{E} = 2.4\text{e-}2$ with $(\alpha, \epsilon) = (0.22, 0.075)$. As can be seen from the results, the proposed method can be utilized to account for the transition pathway and compute critical nuclei between different stable states.

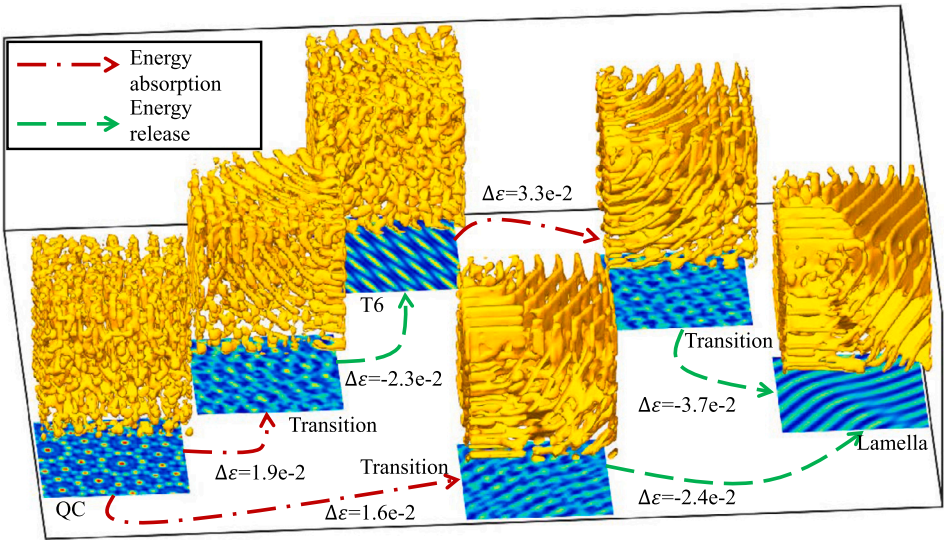

Fig. 9. Dynamic behaviors and transition pathways between different stable order states, including QC to T6, T6 to Lamella, and QC to Lamella, respectively. The sub-figures demonstrate the phase patterns of corresponding crystalline states in 3D space and the projected patterns in the 2D plane. The transferred energy is denoted as $\Delta\mathcal{E}$, whose positive value represents the energy that needs to be absorbed for the transition, and vice versa. The red dashed-dot lines represent the direction of transition caused by the energy absorption and the green dashed lines represent the direction of transition caused by the energy release.

5. Conclusion

In this paper, we reported the efficient computational schemes for the nucleation and transition of quasicrystalline structure, which suffer from anisotropic structural incommensurability and are significant for revealing material properties. Within the framework of the Landau theory, we established two phase field based models to investigate the transition process by taking the variational derivation from the LP energy. In order to avoid the proposed reaction-diffusion system suffering the stiffness caused by the nonlinear terms and falling into the local minima, we modified the two models with the novel Lagrange multiplier method, which were both space and time dependent. The time discretized system was consoled by using the Crank-Nicolson method with a linear form, while the nonlinear terms were solved by taking the Adamm-Bashforth method to hold the second order time accuracy. We adopted the Fourier spectral method with $O(N \log N)$ computational complexity, which can be further applied to GPU-accelerate implementation. To assess the performance of the proposed algorithm, we demonstrate its relative advantages in terms of stability and accuracy compared to the SAV method, IEQ method and the traditional fully-implicit scheme. Putting the method in the larger context of other methods for constructing unconditionally/conditionally stable methods can provide valuable guidance to readers on choosing the appropriate method for phase-field modeling of crystalline structures. We performed various numerical tests to examine the efficiency, accuracy, and robustness of revealing the nucleation and transition of stable quasicrystalline structure.

CRediT authorship contribution statement

Qing Xia: Writing – review & editing, Writing – original draft, Visualization, Software, Methodology, Investigation, Conceptualization. **Junxiang Yang:** Supervision, Software, Methodology, Conceptualization. **Junseok Kim:** Visualization, Supervision, Software. **Yibao Li:** Writing – review & editing, Supervision, Methodology, Funding acquisition, Conceptualization.

Declaration of competing interest

The authors declare that they have no known competing financial interests or personal relationships that could have appeared to influence the work reported in this paper.

Data availability

No data was used for the research described in the article.

Acknowledgement

Y.B. Li is supported by National Natural Science Foundation of China (No. 12271430). The authors are grateful to the reviewers whose valuable suggestions and comments significantly improved the quality of this paper.

References

[1] D. Shechtmann, I. Blech, Metallic phase with long-range orientational order and no translational symmetry, Phys. Rev. Lett. 53 (1984) 1951.
[2] R. Lifshitz, H. Diamant, Soft quasicrystals - why are they stable, Philos. Mag. 87 (2007) 3021–3030.
[3] B. Jiang, Q. Xia, J. Kim, Y. Li, Efficient second-order accurate scheme for fluid-surfactant systems on curved surfaces with unconditional energy stability, Commun. Nonlinear Sci. Numer. Simul. 405 (2024) 108054.
[4] B. Xia, C. Mei, Q. Yu, Y. Li, A second order unconditionally stable scheme for the modified phase field crystal model with elastic interaction and stochastic noise effect, Comput. Methods Appl. Mech. Eng. 363 (2020) 112795.
[5] J. Yin, K. Jiang, A. Shi, P. Zhang, Z. Lei, Transition pathways connecting crystals and quasicrystals, Proc. Natl. Acad. Sci. USA 118 (2021) e2106230118.
[6] Q. Xia, G. Sun, K. Junseok, Y. Li, Multi-scale modeling and simulation of additive manufacturing based on fused deposition technique, Phys. Fluids 35 (2023) 3.
[7] G. Pupillo, P. Ziherl, F. Cinti, Quantum cluster quasicrystals, Phys. Rev. B 101 (2020) 134522.
[8] L. Zhang, W. Ren, A. Samanta, Q. Du, Recent developments in computational modelling of nucleation in phase transformations, NPJ Comput. Mater. 2 (2016) 1–9.
[9] J. Cheng, Q. Xia, K. Junseok, Y. Li, An efficient linear and unconditionally stable numerical scheme for the phase field sintering model, Commun. Nonlinear Sci. Numer. Simul. 127 (2023) 107529.
[10] X. Zeng, G. Ungar, Y. Liu, V. Percec, A. Dulcey, J. Hobbs, Supramolecular dendritic liquid quasicrystals, Nature 428 (2004) 157–160.
[11] Y. Chan, C. Chan, Z. Liu, Photonic band gaps in two dimensional photonic quasicrystals, Phys. Rev. Lett. 80 (1998) 956.
[12] T. Eisenhammer, Quasicrystal films: numerical optimization as a solar selective absorber, Thin Solid Films 270 (1995) 1–5.
[13] J. Dubois, S. Kang, Y. Massiani, Application of quasicrystalline alloys to surface coating of soft metals, J. Non-Cryst. Solids 153–154 (1993) 443–445.
[14] J. Dubois, S. Kang, P. Archambault, B. Colleret, Thermal diffusivity of quasicrystalline and related crystalline alloys, J. Mater. Res. 8 (1993) 38–43.
[15] J. Dubois, Properties- and applications of quasicrystals and complex metallic alloys, Chem. Soc. Rev. 41 (2012) 6760–6777.
[16] Y. Li, Q. Xia, S. Kang, S. Kwak, K. Junseok, A practical algorithm for the design of multiple-sized porous scaffolds with triply periodic structures, Math. Comput. Simul. 220 (2024) 481–495.
[17] A. Archer, A. Rucklidge, E. Knobloch, Quasicrystalline order and a crystal-liquid state in a soft-core fluid, Phys. Rev. Lett. 111 (2013) 165501.
[18] E. Asadi, M. Zaeem, A review of quantitative phase field crystal modeling of solid-liquid structures, JOM 67 (336) (2015) 186–201.
[19] T. Dotera, T. Oshiro, P. Ziherl, Mosaic two-lengthscale quasicrystals, Nature 506 (2014) 208–211.
[20] A. Finney, M. Salvalaglio, Theoretical and computational approaches to study crystal nucleation from solution, ChemRxiv, preprint, https://doi.org/10.26434/chemrxiv-2023-rb79v, 2023.
[21] S. Prestipino, A. Laio, E. Tosatti, Systematic improvement of classical nucleation theory, Phys. Rev. Lett. 108 (2012) 225701.
[22] S. Stoyanov, On the atomistic theory of nucleation rate, Thin Solid Films 18 (1973) 91–98.
[23] Q. Xia, J. Zhu, Q. Yu, K. Junseok, Y. Li, Triply periodic minimal surfaces based topology optimization for the hydrodynamic and convective heat transfer, Commun. Nonlinear Sci. Numer. Simul. 131 (2024) 107819.
[24] K. Burke, Perspective on density functional theory, J. Chem. Phys. 136 (2012) 150901.
[25] Q. Xia, Q. Yu, Y. Li, A second-order accurate, unconditionally energy stable numerical scheme for binary fluid flows on arbitrarily curved surfaces, Comput. Methods Appl. Mech. Eng. 384 (2021) 113987.
[26] V. Kalikmanov, Nucleation theory, in: Classical Nucleation Theory, Springer Netherlands, Dordrecht, 2012, pp. 17–41.
[27] Q. Xia, X. Jiang, Y. Li, A modified and efficient phase field model for the biological transport network, J. Comput. Phys. 488 (2023) 112192.
[28] Y. Han, Y. Hu, P. Zhang, L. Zhang, Transition pathways between defect patterns in confined nematic liquid crystals, J. Comput. Phys. 396 (2019) 1–11.
[29] K. Jiang, P. Zhang, Numerical methods for quasicrystals, J. Comput. Phys. 256 (2014) 428–440.
[30] D. Cao, J. Shen, J. Xu, Computing interface with quasiperiodicity, J. Comput. Phys. 424 (2021) 109863.
[31] Y. Li, C. Luo, B. Xia, J. Kim, An efficient linear second order unconditionally stable direct discretization method for the phase-field crystal equation on surfaces, Appl. Math. Model. 67 (2019) 477–490.
[32] K. Cheng, C. Wang, S. Wise, An energy stable BDF2 Fourier pseudo-spectral numerical scheme for the square phase field crystal equation, Commun. Comput. Phys. 26 (2019) 1335–13645.
[33] H. Lee, A new conservative Swift-Hohenberg equation and its mass conservative method, J. Comput. Appl. Math. 375 (2020) 112815.
[34] Q. Li, L. Mei, B. You, A second-order, uniquely solvable, energy stable BDF numerical scheme for the phase field crystal model, Appl. Numer. Math. 134 (2018) 46–65.
[35] Q. Xia, Y. Liu, K. Junseok, Y. Li, Binary thermal fluids computation over arbitrary surfaces with second-order accuracy and unconditional energy stability based on phase-field model, J. Comput. Appl. Math. 433 (2023) 115319.
[36] R. Lifshitz, D. Petrich, Theoretical model for Faraday waves with multiple-frequency forcing, Phys. Rev. Lett. 79 (1997) 1261.
[37] J. Swift, P. Hohenberg, Hydrodynamic fluctuations at the convective instability, Phys. Rev. A 15 (1977) 319.
[38] M. Cross, P. Hohenberg, Pattern formation outside of equilibrium, Rev. Mod. Phys. 65 (1993) 851.
[39] Y. Li, J. Kim, An efficient and stable compact fourth-order finite difference scheme for the phase field crystal equation, Comput. Methods Appl. Mech. Eng. 319 (2017) 194–216.
[40] M. Uzunca, B. Karasözen, Linearly implicit methods for Allen-Cahn equation, Appl. Math. Comput. 450 (2023) 127984.
[41] Q. Xia, J. Yang, Y. Li, On the conservative phase-field method with the N-component incompressible flows, Phys. Fluids 35 (2023) 1.
[42] K. Cheng, C. Wang, S. Wise, X. Yue, A second-order, weakly energy-stable pseudo-spectral scheme for the Cahn–Hilliard equation and its solution by the homogeneous linear iteration method, J. Sci. Comput. 69 (2016) 1083–1114.
[43] C. Elliott, A. Stuart, The global dynamics of discrete semilinear parabolic equations, SIAM J. Numer. Anal. 30 (1993) 1622–1663.
[44] X. Yang, Linear, first and second-order, unconditionally energy stable numerical schemes for the phase field model of homopolymer blends, J. Comput. Phys. 327 (2016) 294–316.
[45] Q. Cheng, C. Liu, J. Shen, A new Lagrange multiplier approach for gradient flows, Comput. Methods Appl. Mech. Eng. 367 (2020) 113070.
[46] Q. Li, N. Cui, S. Zheng, L. Mei, A new Allen-Cahn type two-model phase-field crystal model for fcc ordering and its numerical approximation, Appl. Math. Lett. 132 (2022) 108211.
[47] P. Subramanian, D. Ratliff, A. Rucklidge, A. Archer, Density distribution in soft matter crystals and quasicrystals, Phys. Rev. Lett. 126 (2021) 218003.
[48] D. Lee, J. Kim, Comparison study of the conservative Allen-Cahn and the Cahn-Hilliard equations, Math. Comput. Simul. 119 (2016) 35–56.
[49] Z. Tan, L. Chen, J. Yang, Generalized Allen-Cahn-type phase field crystal model with FCC ordering structure and its conservative high-order accurate algorithm, Comput. Phys. Commun. 286 (2023) 108656.
[50] J. Shen, J. Xu, J. Yang, The scalar auxiliary variable (SAV) approach for gradient flows, J. Comput. Phys. 353 (2018) 407–416.
[51] F. Guillén-González, G. Tierra, On linear schemes for a Cahn–Hilliard diffuse interface model, J. Comput. Phys. 234 (2013) 140–171.
[52] J. Zhu, L. Chen, J. Shen, V. Tikare, Coarsening kinetics from a variable mobility Cahn–Hilliard equation-application of semi-implicit Fourier spectral method, Phys. Rev. E 60 (1999) 3564–3572.
[53] J. Shen, X. Yang, Numerical approximations of Allen-Cahn and Cahn-Hilliard equations, Discrete Contin. Dyn. Syst. 28 (2010) 1669–1691.
[54] Z. Huang, G. Lin, A. Ardekani, A consistent and conservative phase-field model for thermo-gas-liquid-solid flows including liquid-solid phase change, J. Comput. Phys. 449 (2022) 110795.

[55] Z. Huang, G. Lin, A. Ardekani, Consistent and conservative scheme for incompressible two-phase flows using the conservative Allen-Cahn model, J. Comput. Phys. 420 (2020) 109718.
[56] V. Heinonen, K. Burns, J. Dunkel, Quantum hydrodynamics for supersolid crystals and quasicrystals, Phys. Rev. A 99 (2019) 063621.
[57] Q. Du, L. Ju, X. Li, Z. Qiao, Maximum principle preserving exponential time differencing schemes for the nonlocal Allen–Cahn equation, SIAM J. Numer. Anal. 57 (2019) 875–898.
[58] J. Shen, T. Tang, J. Yang, On the maximum principle preserving schemes for the generalized Allen–Cahn equation, Commun. Math. Sci. 14 (2016) 1517–1534.
[59] Q. Huang, W. Jiang, J. Yang, C. Yuan, A structure-preserving, upwind-SAV scheme for the degenerate Cahn–Hilliard equation with applications to simulating surface diffusion, J. Sci. Comput. 97 (2023) 64.
[60] Q. Cheng, J. Shen, A new Lagrange multiplier approach for constructing structure preserving schemes, II. Bound preserving, SIAM J. Numer. Anal. 60 (2022) 970–998.
[61] G. Tierra, F. Guillén-González, Numerical methods for solving the Cahn–Hilliard equation and its applicability to related energy-based models, Arch. Comput. Methods Eng. 22 (2015) 269–289.
[62] R. Bailo, J. Carrillo, S. Kalliadasis, S. Perez, Unconditional bound-preserving and energydissipating finite-volume schemes for the Cahn–Hilliard equation, Commun. Comput. Phys. 34 (2023) 713–748.
[63] W. Ostwald, Studies on the formation and change of solid matter, Z. Phys. Chem. 22 (1897) 289–330.